

Computer Simulation of Helium Effects in Plutonium During the Aging Process of Self-Radiation Damage

Bingyun Ao^{1,*}, Piheng Chen¹, Peng Shi¹, Xiaolin Wang¹, Wangyu Hu² and Liang Wang²

¹ National Key Laboratory for Surface Physics and Chemistry, Mianyang, Sichuan 621907, China.

² Department of Applied Physics, Hunan University, Changsha 410082, China.

Received 29 June 2010; Accepted (in revised version) 21 January 2011

Communicated by Zhengming Sheng

Available online 29 November 2011

Abstract. Due to α radioactive decay Pu is vulnerable to aging. The behavior of He in Pu is the foundation for understanding Pu self-radiation damage aging. Molecular dynamics technique is performed to investigate the behavior of defects, the interaction between He and defects, the processes of initial nucleation and growth of He bubble and the dependence of He bubble on the macroscopical properties of Pu. Modified embedded atom method, Morse pair potential and the Lennard-Jones pair potential are used for describing the interactions of Pu-Pu, Pu-He and He-He, respectively. The main calculated results show that He atoms can combine with vacancies to form He-vacancy cluster (i.e., the precursor of He bubble) during the process of self-radiation as a result of high binding energy of an interstitial He atom to vacancy; He bubble's growth can be dominated by the mechanism of punching out of dislocation loop; the swelling induced by He bubble is very small; grain boundaries give rise to an energetically more favorable zone for the interstitial He atom and self-interstitial atom accumulation than for vacancy accumulation; the process of He release can be identified as the formation of release channel induced by the cracking of He bubble and surface structure.

PACS: 61.72.-y, 61.72.Cc, 61.72.Qq, 71.15.Pd

Key words: Plutonium, radiation damage, helium effect, molecular dynamics, crystal defect.

1 Introduction

Pu is perhaps the most complex metallic element known and has attracted extraordinary scientific interest since its discovery in 1941. It is of great technological importance due

*Corresponding author. *Email addresses:* aobingyun24@yahoo.com.cn (B. Y. Ao), chenph@live.cn (P. H. Chen), shipeng2009@gmail.com (P. Shi), xlwang@caep.ac.cn (X. L. Wang), wangyuhu2001cn@yahoo.com.cn (W. Y. Hu), wangliang0329@gmail.com (L. Wang)

to its use in nuclear industry. However, modern day problems concerning Pu involve understanding and predicting the properties of Pu and its alloys for the safe handling, use and long-term storage of these important, but highly toxic materials which made experimental observations extremely difficult [1]. So, development of a predictive aging model for Pu is one of major goals of many researchers' works on Pu. Pu is vulnerable to aging because it is a radioactive element, decaying to U by emitting α particle. Although the widely used Pu-239 has a relatively long half-life of about 24,000 years, its decay rate is still sufficiently high to lead to a significant buildup of He and radiation damage within the metal after several decades [2]. As for the behavior of He atoms in Pu lattice, there may be a number of interactions occurring in the lattice. These interactions mainly include: 1) trapping and thermal detrapping of He atom in single vacancy, divacancies and vacancy clusters; 2) He atom trapping at dislocations and grain boundaries; 3) replacement of He atom bound to single vacancy by either interstitial Pu atoms or U atoms or other impurities; 4) He atom clustering into He-vacancy clusters and He bubble; 5) displacement of trapped He atoms by He-He or He-U collisions; and 6) diffusion of He atom as an interstitial [3]. Knowledge from Pu and other materials suffered from He and radiation damage has proved the degradation, or even worse, the invalidation of the material properties [4]. In fact, He effects in Pu are always associated with radiation damage effects and can be regarded as the focalization on probing the microstructural changes with ages.

Despite the central importance, there are still dearth of comprehensive studies in the literature concerning the complex He effects in Pu. Experimentally, transmission electron microscope (TEM), positron annihilation spectroscopy (PAS), X-ray diffraction (XRD), dilatometry, etc. have been used to probe into the He effects in Pu [5–7]. Although, these pioneering researches provide some valuable evidences on understanding the initial stage of He bubble nucleation and growth, many uncertainties still exist as a result of difficulties in experiments and lacking sufficient aged Pu samples. On the other hand, more and more theoretical modeling techniques have been performed to explore the atomistic mechanism of cascade damage effects during the last two decades [8,9]. However, the atomistic behaviors of He effects have not been studied in detail with few exceptions, among them the classical works of Valone et al. and Dremov et al. who studied the stabilities of isolated He bubbles in δ Pu-Ga alloys by molecular dynamics simulation [10, 11]. They found that the stabilities of He bubble were strongly dependant on size, He-vacancy ratio and temperature. As for the macroscopical aspects of He bubble in Pu such as lattice swelling, material property changes, He bubble pressure and He release, there are few reports to the best of our knowledge.

In this article, we review our recent findings on He effects in Pu during the aging process of self-radiation damage by computer simulation technique, especially on investigating the microcosmic mechanism of initial nucleation and formation of He bubble. In addition, some macroscopical aspects of He bubble in Pu such as lattice swelling, He bubble pressure and He release process are also presented [12–14]. The remainder of the paper is organized as follows. In Section 2, the methods used are briefly described focus-

ing on the development of interatomic potentials. The models for different simulations and calculations are discussed in Section 3. Finally, conclusive comments are provided in Section 4.

2 Methods

2.1 Molecular dynamics

A complete understanding of the behavior of He in Pu requires an atomic level simulation. Molecular dynamics (MD) simulation is an important tool for understanding materials at atomic level. By using MD simulation, the behavior of defects in solid materials can be directly probed. The general methods of MD simulation have been discussed in great details by a number of authors; thus, we give here only the specific details of our calculations. In the present MD simulation, the six-value Gear predictor-corrector algorithm is employed. Usually, the time step is chosen as 1fs and total simulation time is greater than 10ps. In some cases, for instance the computational system contains nanometer-size He bubbles and extended defects, the total simulation time is high to ns level, depending on the computational cell being simulated. The thermodynamic quantities are evaluated only after ensuring a thorough equilibration of the computational system. Periodic computational cells are used to eliminate surface effects. The detailed simulation processes for different investigations will be addressed in the following text.

2.2 Potentials

The success of the MD simulation lies in the choice of the interatomic potentials of Pu-Pu and Pu-He. We have developed our own Pu embedded atom method (EAM) potential to reproduce the fcc δ Pu phase. In the original EAM model, there are two assumptions [15]. First, the atomic electron densities are to be well represented by the spherically averaged free atom densities calculated from Hartree-Fock theory. Second, the host electron density is approximated by a linear superposition of the atomic densities of the constituents. These assumptions are too simple and cannot describe the actual situation well. Baskes modified it to include direct and bonding in the expression of electron density, and applied to variety of cubic materials [16], and the calculations were very complicated. Our group proposed another modified method [17]. With introducing a modified energy term $M(P)$ to the total energy expression to express the energy difference resulting from the electron density difference and to correct the negative Cauchy relation, a new type of modified analytic EAM (MAEAM) has been constructed for many typical metals and alloys [18–23].

The present MAEAM describes the total energy E_t of any structure as the sum of three terms, a many-body term depending on the local electron density, a two-body term depending on interatomic distances, and a modification term to correct for the assumption

of the linear superposition of atomic electron density in the original EAM [20–23],

$$E_t = \sum_i F(\rho_i) + \frac{1}{2} \sum_{i,j} \phi(r_{ij}) + \sum_i M(P_i), \quad \text{for } i \neq j, \quad (2.1)$$

where $\phi(r)$ is the effective two-body potential, $F(\rho)$ is the embedding energy. The local electron density ρ_i and its second order P_i are determined by a superposition of individual atomic electron densities $f(r_{ij})$,

$$\rho = \sum_m f(r_m), \quad (2.2a)$$

$$P = \sum_m f^2(r_m), \quad (2.2b)$$

where m is the number of the neighbor atoms. The atomic electron density is described by the function $f(r)$,

$$f(r) = \left(\frac{r_1}{r}\right)^{4.7} \left[\frac{r_{ce}-r}{r_{ce}-r_1}\right]^2, \quad (2.3)$$

where r_1 is the nearest neighbor atomic equilibrium distance, $f(r)$ is truncated at r_{ce} , $r_{ce} = r_4 + 0.75(r_5 - r_4)$, where r_4 and r_5 are the fourth and fifth neighbor distances for a perfect crystal, respectively.

The energy modification term is empirically taken as,

$$M(P) = \alpha \left\{ 1 - \exp \left[-10^4 \left(\ln \frac{P}{P_e} \right)^2 \right] \right\}, \quad (2.4)$$

where P_e is its equilibrium value.

The embedding functions of $F(\rho)$ take the same forms as those used by Johnson [24],

$$F(\rho) = -F_0 \left[1 - n \ln \frac{\rho}{\rho_e} \right] \left(\frac{\rho}{\rho_e} \right)^n, \quad (2.5)$$

where F_0 and n are model parameters, ρ_e is the equilibrium electron density.

A Morse-like pair potential is proposed in the frame of our MAEAM. The proposed pair potential $\phi(r)$ is,

$$\begin{aligned} \phi(r) = & k_0 + k_1 \exp \left(1 - \frac{r}{r_1} \right) + k_2 \exp \left[2 \left(1 - \frac{r}{r_1} \right) \right] + k_3 \exp \left[3 \left(1 - \frac{r}{r_1} \right) \right] \\ & + k_4 \exp \left[4 \left(1 - \frac{r}{r_1} \right) \right] + k_{-1} \exp \left(\frac{r_1}{r} - 1 \right), \end{aligned} \quad (2.6)$$

where k_i ($i = -1, 0, 1, 2, 3, 4$) are the potential parameters. In the present model, the atomic interactions up to the third neighbor distance are considered and $\phi(r)$ is truncated between the third and the fourth neighbor distance, $r_c = r_3 + 0.75(r_4 - r_3)$. At this point, the pair potential and its slope are zero, i.e.,

$$\phi(r_c) = 0, \quad \phi'(r_c) = 0. \quad (2.7)$$

Table 1: Input physical parameters for the δ Pu MAEAM potential, a is the lattice constant, E_c the cohesive energy, E_{1f} the mono-vacancy formation energy, C_{11} , C_{12} and C_{44} the elastic constants.

a (nm)	E_c (eV)	E_{1f} (eV)	C_{11} (GPa)	C_{12} (GPa)	C_{44} (GPa)
0.464	-4.20	0.90	38.0	26.0	33.0

All the model parameters are determined analytically by fitting the properties of metals, such as lattice constants a , cohesive energy E_c , mono-vacancy formation energy E_{1f} , and elastic constants C_{11} , C_{12} , C_{44} . The input physical parameters for Pu [25–27] are listed in Table 1. Although this potential is for pure Pu, the elastic constants and the mono-vacancy formation energy are taken from the Ga-stabilized Pu alloy. The Pu EAM potential has been proven to be effective to a certain extent to reproduce many solid properties of Pu, but it can not reproduce the complicated phase transformations [26,28–30] and can not reproduce the unusual phonon softening in δ Pu. In fact, many of these difficulties can be corrected only by the most advanced electronic structure calculation methods, for example, the recently developed dynamics mean field theory (DMFT) has been succeeded in reproducing the unusual phonon softening in δ -phase Pu [27,31]. From the viewpoint of atomic level computer simulation, the Pu MAEAM potential can be tentatively used to investigate the atomic behavior of defects in Pu.

The He-He potential used is of the Lennard-Jones pair potential [32],

$$\phi = \phi_0 \left[\left(\frac{r_0}{r} \right)^{12} - 2 \left(\frac{r_0}{r} \right)^6 \right], \quad (2.8)$$

where ϕ_0 and r_0 are the potential parameters. The He-He potential has been widely used to study He effects in solid materials.

For the Pu-He cross potential, there is no experimental data at all with which to fit the potential. As is well known, He atom has a filled-shell electronic configuration and are thus likely to interact with other atoms in a simpler way than do metal atoms, in other words, the electronic effects of He-metals interactions may be negligible. For this reason, the Pu-He cross potential is modeled as Mores pair potential,

$$\phi = \phi_0 \left[\exp \left(-2\alpha \left(\frac{r}{r_0} - 1 \right) \right) - 2 \exp \left(-\alpha \left(\frac{r}{r_0} - 1 \right) \right) \right], \quad (2.9)$$

where ϕ_0 , r_0 and α are the potential parameters. In order to determine the potential parameters, we try to compare Pu with other fcc metals (such as Al, Pd and Ni) whose interaction potentials with He were developed by using first-principles calculations [33]. We have obtained the potential parameters by choosing from a variety of values of ϕ_0 , r_0 and α . Although the fidelity of the potential parameters is limited, the Pu-He cross potential is qualitatively feasible for modeling the behavior of He in Pu. Furthermore, the selected potential parameters are in accordance with the Pu-He dimer potential developed by using *ab initio* calculations [34]. In fact, with view to the importance of Pu-He potential for the atomistic investigation of He behavior and the lack of experimental data

on Pu-He system, we are developing the Pu-He potential from the first-principles energy band calculation method [35,36].

3 Results and discussion

3.1 Energetic calculation of He-vacancy cluster

In terms of Trinkaus's classification of He bubble by size, the lowest size class is usually indicated by He-vacancy (He_nV_m , n and m denote the number of He atoms and vacancy, respectively) clusters, which may play an important role in the nucleation of He bubble [37,38]. Such small He_nV_m clusters are hardly characterized experimentally, which should be necessary for a theoretical approach.

The defects formation energies are determined by comparing the energy of a crystal containing defects with a crystal of the same number of atoms on their perfect lattice sites. The formation energy of a He_nV_m cluster that contains n He atoms and m vacancies is defined as follows,

$$E_f(\text{He}_n\text{V}_m) = E_{tot}(\text{He}_n\text{V}_m) - n\varepsilon_{\text{He}} - (N-m)\varepsilon_{\text{Pu}}, \quad (3.1)$$

where $E_f(\text{He}_n\text{V}_m)$ is the formation energy of He_nV_m cluster with n He atoms in a void of m vacancies, $E_{tot}(\text{He}_n\text{V}_m)$ is the calculated total energy of a computational Pu cell containing a He_nV_m cluster, ε_{Pu} is the cohesive energy of a perfect fcc Pu crystal, and ε_{He} is the cohesive energy of a perfect fcc He crystal. Here, the calculated cohesive energies of perfect crystals are -4.2eV/atom and -0.0071eV/atom for Pu and He, respectively. N denotes the number of perfect fcc lattice sites in the computational cell and therefore $(N-m)$ is the number of Pu atoms in the cell. The solubility of He in Pu is described by the binding energies of a He atom $E_B(\text{He})$ to a He_nV_m cluster, which are calculated from the following equation [39],

$$E_B(\text{He}) = E_f(\text{He}_{n-1}\text{V}_m) + E_f(\text{He}) - E_f(\text{He}_n\text{V}_m), \quad (3.2)$$

where $E_f(\text{He})$ is the formation energy of He in an interstitial site. The structure of the empty void is determined by beginning with a single vacancy, and repeatedly removing the atom having the highest potential energy from the cell, thereby creating another vacancy for calculating the isolated vacancy formation energy, so the formation energy of di-vacancy is calculated. By repeating the step in the same manner, the vacancies are increased one by one and the formation energy of an empty void is obtained as a function of the number of vacancy in the void. Afterwards, a He atom is firstly introduced into an m -size void V_m for calculating the formation energy of He_1V_m cluster, then the He atoms are introduced into the cluster one by one for calculating the formation energies of the clusters containing increasing He atoms. In order to fully relax the simulation cell, annealing molecular dynamics is employed for each initial configuration. The computational system is relaxed at 300K, with the temperature controlled via explicit rescaling

of the velocities and the pressure controlled using Parrinello and Rahman method [40], followed by slowly cooling and quenching the system to 0K. The positions of the atoms are relaxed to their minimum energy configurations. The forces exerted on each atom are calculated, and then the formation energies of He_nV_m clusters are calculated.

3.1.1 Formation energies of He_nV_m clusters

The formation energies of He_nV_m clusters are the foundation of calculating the defect binding energies. Fig. 1 shows the dependence of the formation energies of He_nV_m clusters on the number of He atom. It can be found that for He atom in Pu lattice, the formation energies of He_nV_m clusters slowly increase with the introducing of He atom until the ratio of the number of He atom to vacancy is greater than 1, which indicates the lowest energy configuration occurs when there is one vacancy per He atom. Fig. 2 shows the dependence of the formation energies of He_nV_m clusters on the number of vacancies. The formation energies of He_nV_m clusters slowly decrease with the introducing of vacancy until the ratio of the number of He atom to vacancy is greater than 1, which also indicates the lowest energy configuration occurs when there is one vacancy per He atom. When the He-to-vacancy ratio (n/m) of a cluster is less than 1, the formation energy of the cluster is close to the void formation energy. However, when n/m is greater than 1, the rapid increase of the formation energy is mainly due to the presence of He. In this way, the cluster size dependence of the formation energy of a He_nV_m cluster is greatly dependent on the ratio, n/m .

3.1.2 Binding energies of point defects to He_nV_m clusters

According to the Eq. (3.2), the binding energies of a He atom to a He_nV_m cluster have been calculated. These binding energies are graphed in Fig. 3. He density is defined as the He to vacancy ratio of the He_nV_m cluster, which is provided by n/m . As shown in the figure, the binding energies indicate a strong dependence on the He density. He binding energy represents the energy required to bind the n^{th} He atom in a He_nV_m cluster. Notes that for the smaller ratio of n/m , the binding energy approximately equals to the formation energy of an interstitial He atom in Pu lattice. It shows that He atom is most strongly bound to the large nearly empty voids, because He exists in a nearly free state. The high binding energies also explain the formation of He bubbles. The binding energy of an interstitial He atom to He_nV_m clusters gradually decreases with increasing He density, followed by an increase at He density greater than 5. As illuminated by Morishita et al. [38], the change in the dependence of the energies on the He density at greater than 5 may be originated from the athermal SIAs production and associated effective decrease in the He density. In other words, the collective motion of He atoms in the cluster produces bubble pressure large enough to push the Pu atoms off from their normal lattice sites and spontaneously creates addition vacancies and SIAs, therefore increasing the bubble volume and thus lowering the He density. The process is more like the self-trapping mechanism of He bubble formation in the perfect crystal. In fact, our present studies have shown that five He atoms cluster together in a perfect Pu lattice is sufficient to

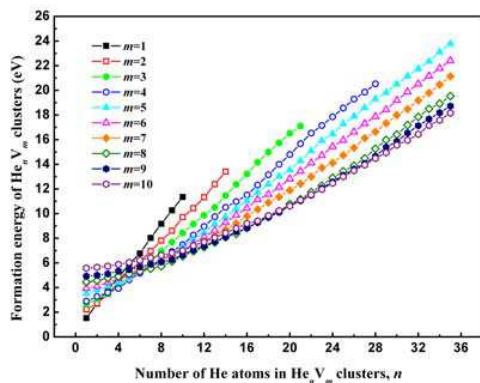


Figure 1: $He_n V_m$ formation energy as a function of the number of He atoms.

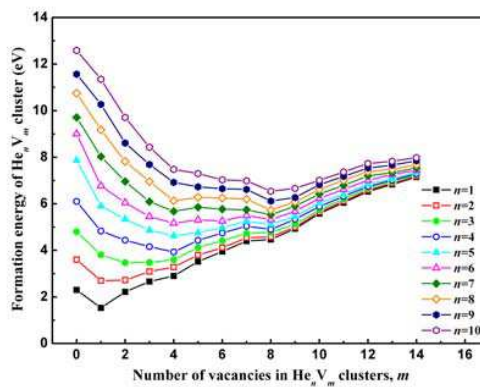


Figure 2: $He_n V_m$ formation energy as a function of the number of vacancies.

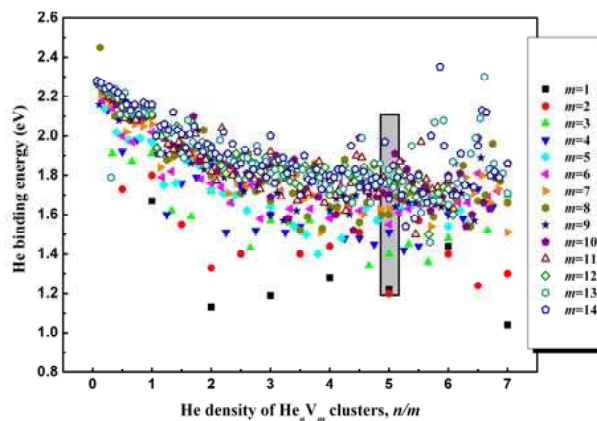


Figure 3: Binding energy of a He atom to $He_n V_m$ clusters as a function of the He density of the clusters.

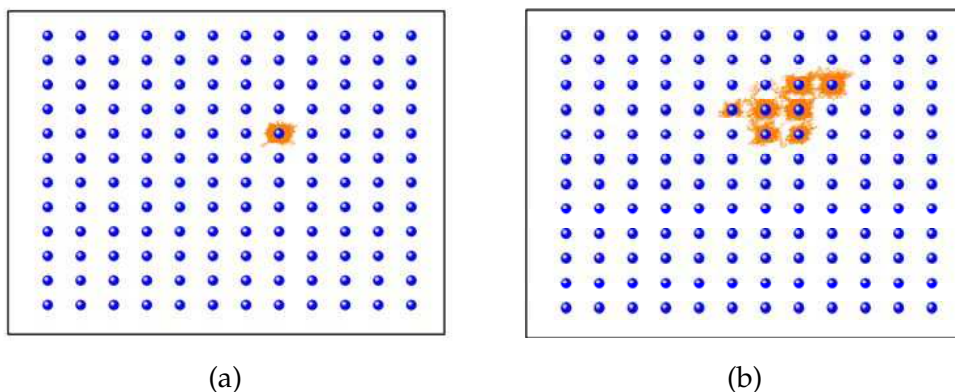


Figure 4: Trajectory of one He atom in the perfect Pu lattice at different temperatures: (a) 300K; (b) 400K. In the figure, orange lines are the trajectory of He atom; blue balls are the initial Pu atomic positions of one layer which is provided to make the jump of He atoms clear.

spontaneously push a Pu atom off from its normal site, thereby creating a Frenkel pair and a deeply-bound He cluster. The introduction of further He atoms produces more Frenkel pairs. The results indicate that the maximum n/m ratio in a He_nV_m cluster is about 5. This athermal behavior may effectively increase the number of vacancies in the cluster, consequently, reduce the actual He density of the cluster.

3.2 He diffusion in perfect lattice

He diffusion in metals is still a matter of investigation, and yet still requires a deeper fundamental understanding. It is a basic requirement for bubble nucleation and growth, and it is the result of random jumps of He atoms from one to another (meta-) stable lattice site. The most important positions for He atoms in a lattice are interstitial and substitutional sites (He atom in a vacancy). The preferential position and dominant migration mode depend on temperature as well as on the presence of other intrinsic or radiation induced defects acting as traps for He atoms [41]. For example, above results have shown that He can strongly bind to vacancies and He_nV_m clusters and some extended defects such as dislocations and grain boundaries generally represent fast diffusion paths for He atoms.

Our present works aim to simulate the diffusion process of one He atom in the perfect Pu lattice by using MD technique. Due to the size effect and the energy difference for He atom in the perfect lattice, He atom at octahedron interstitial site is more stable than at tetrahedron interstitial site, thus the diffusion process can be seen as He atom moves from one octahedron interstitial site to another. To make the procedure simple, He atom migration can be treated as He atom "jumps" from one octahedron interstitial site to the first neighbor one. During the simulation, the jump number of He atom is recorded and the diffusion coefficient can be calculated from the jump-frequency method which is derived from Einstein relation as follow and very suitable for the interstitial diffusion in perfect lattice [42,43],

$$D = f \frac{\alpha^2}{2d'} \quad (3.3)$$

where D is the diffusion coefficient of a He atom, f is the jump frequency, α is the jump distance, d is the diffusion dimension, in our simulation, $d = 3$. At the beginning of MD simulation, He atom is placed near the center of the simulation cell. At relatively low temperature, He atom oscillates around its initial octahedron interstitial site, as is depicted in Fig. 4(a). When the temperature is increased to 400K, there are several relatively stable octahedron interstitial sites for He atom, as is shown in Fig. 4(b). It is obvious that He atom obtain enough thermal energy to jump across the potential barrier, so the diffusion process occurs. The temperature at which He atom begins to jump in Pu is much lower than in other fcc metal, such as Pd and Ni (the corresponding temperatures are about 800K and 600K for Pd and Ni, respectively) [42]. From this result, we may conclude that it is easier for He atom in Pu lattice than in Ni and Pd lattices to form a bubble. In fact,

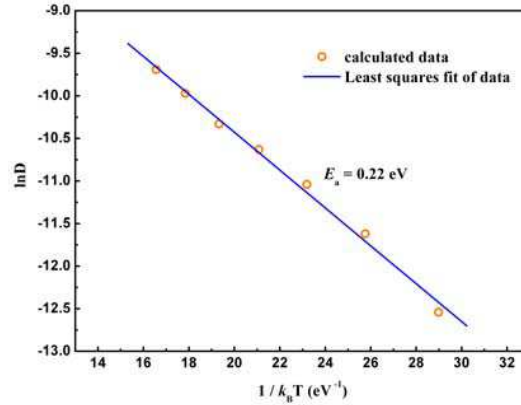


Figure 5: Arrhenius plot of the diffusion coefficient of interstitial He atom in Pu.

the high mobility of He atom in Pu lattice implies that the activation energy for He atom diffusion is correspondingly low, which will be proven in the followings.

The diffusion coefficient D can be calculated from the jump-frequency method. On the other hand, we know the Arrhenius relation as follows,

$$\ln D = \ln D_0 - \frac{E_a}{k_B T}, \quad (3.4)$$

where E_a is the activation energy of interstitial mechanism for He atom diffusion. With the plot of $\ln D$ to $1/T$ as shown in Fig. 5, the values of $\ln D_0$ and E_a are evaluated as -5.98 and 0.22eV for He atom diffusion in Pu lattice, respectively. This activation energy is far lower than those for He atom diffusion in Pd and Ni lattices which are 0.67eV and 0.49eV, respectively [42]. The temperature dependence of diffusion coefficient of He atom in Pu lattice can be derived as following,

$$D(T) = 0.0025 \exp\left(-\frac{0.22\text{eV}}{k_B T} \text{cm}^2\text{s}^{-1}\right). \quad (3.5)$$

Compared with He atom diffusion in other fcc and bcc metals, He atom diffusion in Pu is fast, which may lead to a rapid accumulation of He atoms at some extended defects resulting in the formation of bubbles, as observed in the [44].

3.3 Interaction between He and grain boundary (GB)

3.3.1 Atomic structures of GB

The interactions between He and GB are investigated within the framework of coincidence site lattice (CSL). Coincidence boundaries are fundamental to current models of grain-boundary structure, and in addition, have a number of simplifying features from the computational standpoint. We first consider the structures of two symmetrical tilt GBs $\Sigma 5(310)[001]$ and $\Sigma 5(210)[001]$ with angles misorientation 36.87° and 53.13° , which

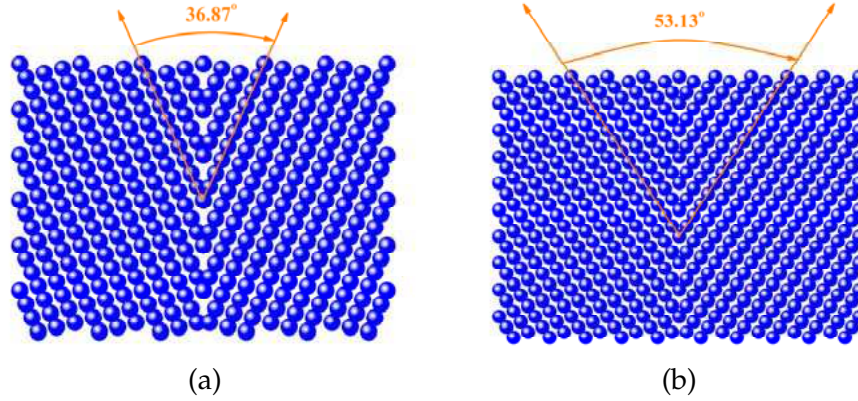


Figure 6: Initial atomic structures of two symmetrical tilt GBs. (a) $\Sigma 5(310)[001] - 36.87^\circ$, (b) $\Sigma 5(210)[001] - 53.13^\circ$.

are well known from experimental observations and computational simulations. The initial unrelaxed-state structures of two GBs are shown in Fig. 6(a) and (b), respectively.

In order to obtain the equilibrium structures of two GBs, annealing MD is employed and periodic boundary conditions are imposed in directions parallel to the GB plane. Each GB contains free atoms, which are able to move under interatomic forces, as well as fixed atoms which are fixed in their lattice sites to maintain the total volume of the computational system. The computational systems are relaxed at 300K, with the temperature controlled via explicit rescaling of the velocities and the pressure controlled using Parrinello and Rahman method, followed by slowly cooling and quenching the systems to 0K. The positions of the atoms are relaxed to their minimum energy configurations. The point defects (including He, vacancy and SIA) are placed at different sites along GB. After static relaxation, the point defect formation energy can be determined by comparing the energy of GB containing a point defect with a GB of the same number of Pu atoms. In the article, we firstly report the results of the interaction between He and GB.

3.3.2 Energetic calculation of He at GB

The interaction between He and GB is investigated by insertion of a single He atom in either an interstitial or a substitutional location along GB, and then relaxing the computational system. The formation energy of the He atom (either interstitial or substitutional) at a particular site s along GB is determined from the equation,

$$E_f^s(\text{He}) = E_c^s(\text{GB}) - E_c(\text{GB}) - \varepsilon_{\text{He}}, \quad (3.6)$$

where $E_c^s(\text{GB})$ and $E_c(\text{GB})$ are the total configuration energies of the relaxed GB with a He atom at site s and without the He atom, respectively. The strength of the interaction between a point defect and a GB is represented by its binding energy. The binding energy of the He atom at the site s to the GB core is calculated from the equation,

$$E_b^s(\text{He}) = E_f(\text{He}) - E_f^s(\text{He}), \quad (3.7)$$

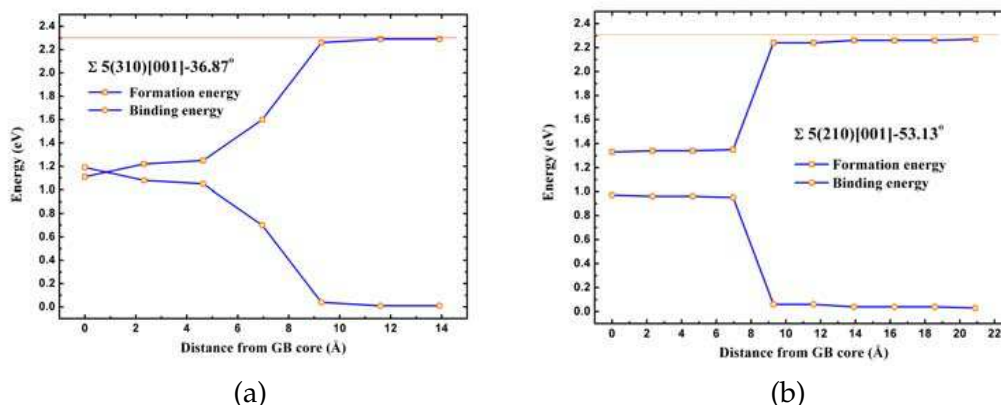


Figure 7: Formation energy and binding energy of interstitial He atom as a function of the distance from the GB core. (a) $\Sigma 5(310)[001]-36.87^\circ$, (b) $\Sigma 5(210)[001]-53.13^\circ$.

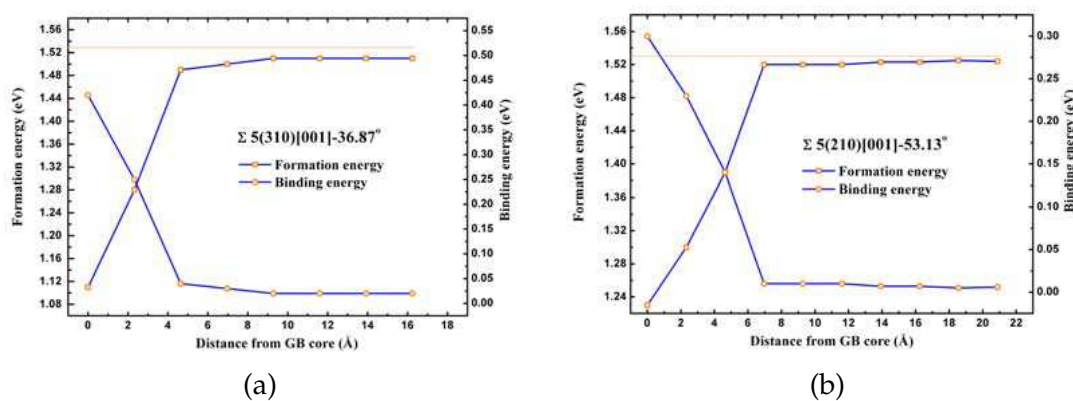


Figure 8: Formation energy and binding energy of substitutional He atom as a function of the distance from the GB core. (a) $\Sigma 5(310)[001]-36.87^\circ$, (b) $\Sigma 5(210)[001]-53.13^\circ$.

where $E_f(\text{He})$ is the formation energy of He atom (either interstitial or substitutional) in the perfect Pu crystal. The calculated values are 2.3eV and 1.53eV for interstitial and substitutional He atoms, respectively.

In Figs. 7 and 8, the formation energy and binding energy of interstitial and substitutional He atoms are plotted as a function of the distance from GB core. The results show that the formation energies are lower than in the perfect crystal but variations from site to site along GB are very remarkable. Both substitutional and interstitial He atoms are trapped at GB, a result similar to the findings of Baskes [45] in fcc Ni and Kurtz [44] in bcc Fe. Interstitial He atom is much more strongly bound at GB core than substitutional He atom (He-vacancy complex) mainly due to the strong binding of the He atom to the vacancy. It is clear that the binding energy of a He atom at GB core is greater than that of a He atom to a vacancy by a few tenth of an electron volt. The binding energies for both interstitial and substitutional He atoms are close to zero at some distances. For the GB

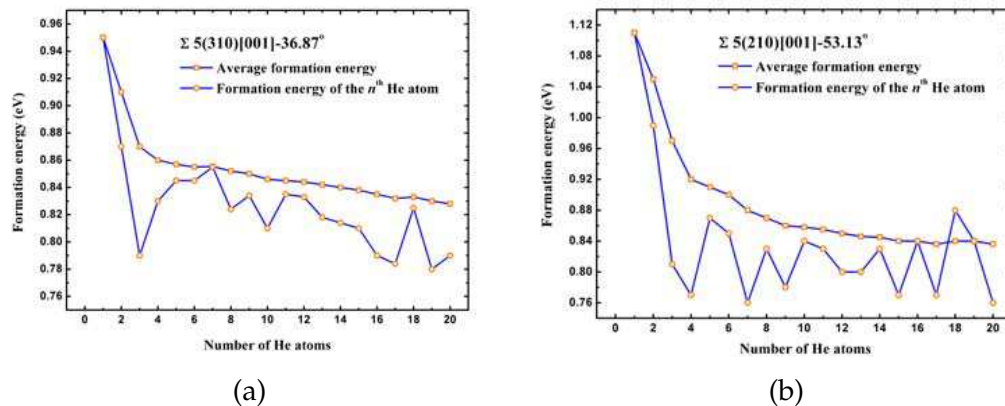


Figure 9: Formation energy of multiple He atoms as a function of the number of He atom. (a) $\Sigma 5(310)[001]$ – 36.87° , (b) $\Sigma 5(210)[001]$ – 53.13° .

$\Sigma 5(310)[001]$, the distances from the GB core, i.e., capture radii, are about 9.2\AA and 4.2\AA for interstitial and substitutional He atoms, respectively. For the GB $\Sigma 5(210)[001]$, the corresponding capture radius are 9.2\AA and 6.5\AA , which implies that the capture radius depend on the GB structures. Further works about the dependence of GB structure on binding He atom are in progress.

The high binding energy of the interstitial He atom at GB indicates that GB is a sink for trapping He atoms. The interactions between a few of He atoms and GB are investigated by adding He atom one by one into GB core. The first He atom is introduced into GB core for calculating the formation energy of single He atom. Afterwards, the second He atom is introduced at the nearest neighbor interstitial site of the first He atom for calculating the formation energies of two He atoms and the second He atom. In this way, 20 He atoms are sequentially introduced into GB core. Fig. 9(a) and (b) show the plots of the average formation energy of He atom and the formation energy of the n^{th} He atom at two GBs versus the number of He atom. As shown in the two figures, the average formation energy and the formation energy of the n^{th} He atom at two GBs slowly decrease with the increasing number of He atom. The results also imply that the average binding energy and the binding energy of the n^{th} He atom at two GBs slowly increase with the increasing number of He atom. From these results, we can conclude that He atoms tend to form bubbles in the GB core. The conclusion is likely to provide perceptive in understanding He embrittlement or He damage in Pu. Researches regarding this problem will focus on He diffusion along GB.

3.4 Growth of He bubble

3.4.1 Punching out dislocation loop

We have found that five He atoms in Pu can cluster by self-trapping mechanism, creating a Frenkel pair and a deeply bound cluster. The introduction of further interstitial He

atoms produces many more Frenkel pairs. After reaching a certain He-vacancy size, the punching out of dislocation loop is energetically more favorable. In fact, the punching out of dislocation can be viewed as the extension of He self-trapping [47].

Experiments have shown that nanometer-size He bubbles form in Pu of at least twenty-year age mainly due to its long half-life of about 24,000 years. Atomic scale MD technique can not be used to investigate the overall process of He bubble formation or even only the process of He_nV_m cluster formation for the inherent deficiency in time-scale. For this reason, we simplify the He bubble formation process by only taking the near equilibrium configuration into consideration, which can be viewed as reasonable to some extent for describing the atomistic behavior of He bubble [2]. The initial configuration of interstitial He atoms in bubble is set to be very sparse. After MD relaxation, most of the He atoms cluster together forming a compact He bubble. Only a few of He atoms are apart from the He bubble, forming some substitutional He atoms and some very small He-vacancy clusters. The dynamics process shows that He bubble forms at the beginning of MD simulation, which implies that initial configuration of interstitial He atoms is very instable and the equilibrium configuration of He bubble is relatively stable. During the process of He bubble growth, many Pu atoms around He bubble are pushed off the normal lattice sites, finally, those Pu atoms form a distinct dislocation loop, i.e., the rectangle of self interstitial Pu atoms around He bubble as shown in Fig. 10.

The most remarkable property of the dislocation loop is that all the Pu atoms inside the dislocation loop still stay at the normal lattice sites while the Pu atoms of the dislocation is disorder. When He bubble is removed and the cell is performed MD simulation again, most of those Pu atoms of dislocation loop approximately come back to their normal lattice sites and only a few of Pu atoms form crowded interstitial atoms. As discussed by many researchers, He bubble in metals may show a packing structure mainly due to crystal stresses. However, the structure of He bubble strongly depends on He atomic density (He-vacancy atomic ratio). We have found that the configuration of He atoms in relatively small He_nV_m cluster shows fcc-like packing when the He atomic density is about less than 5. As for He bubble with high He atomic density, He atoms do not show perfect fcc packing, but He bubble shows a compact ellipsoidal structure, as indicated in Fig. 11.

3.4.2 Lattice swelling by He bubble

The swelling induced by He bubble growth is shown in Fig. 12 as a function of He atomic concentration. The swelling is defined by $S = (V - V_0)/V_0$, where V is the equilibrium volume of the relaxed simulation cell containing a bubble and V_0 is the initial volume in the absence of bubble. For the low He concentration, swelling increases linearly with increasing He concentration. However, swelling does not increase linearly with high He concentration. As is well known, one of very important macroscopical effects of He in metals is swelling due to He bubble formation and growth. As shown in the figure, the swelling induced by He bubble in δ Pu is very small. For δ Pu, the cumulative rate of He production is about 40 atomic parts per million per year (appm/year). Even after

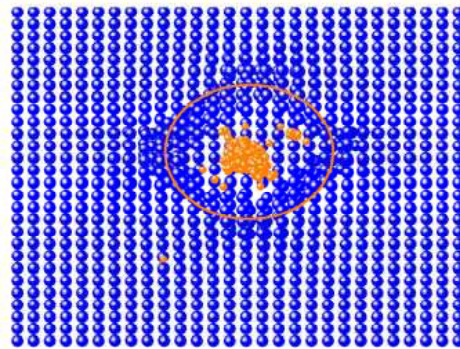


Figure 10: Projection of simulation cell containing a bubble of 216 He atoms. Pu and He atoms are denoted by blue and orange balls, respectively. The dislocation loop is indicated by orange circle.

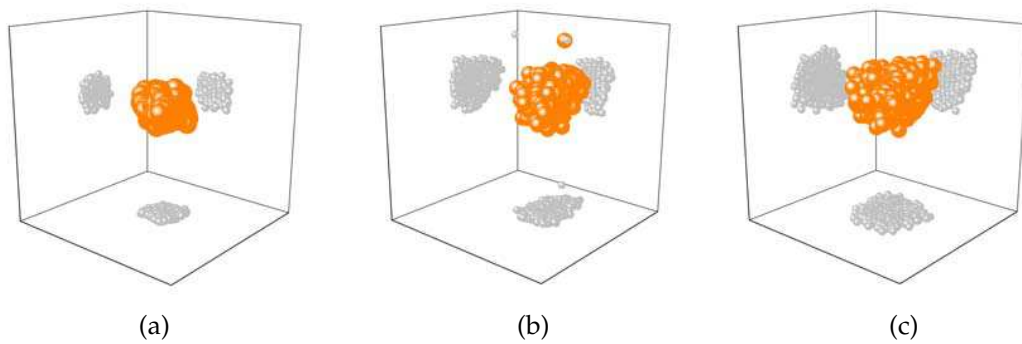


Figure 11: 3D configurations of He bubbles and their projections on three planes. The orange and light gray balls designate He atoms and their projections, respectively. (a) 216 He atoms, (b) 512 He atoms, (c) 800 He atoms.

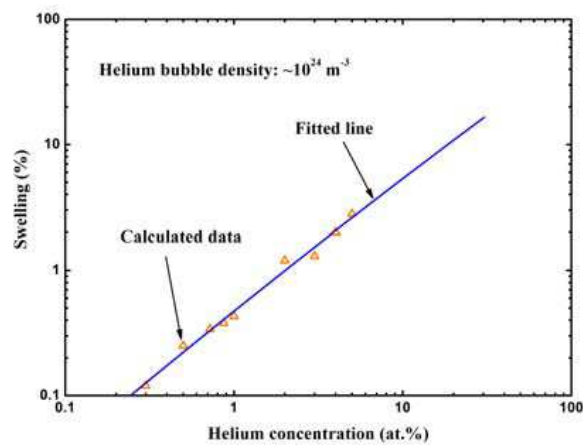


Figure 12: Calculated results for swelling of Pu containing He bubble.

40 years of self-radiation aging, the swelling is still less than 1%. From the calculated results, we can infer that swelling due to He bubble is less serious than other possible mechanism, such as void swelling. In fact, our MD results have indicated that grain boundary and dislocation can act as sinks and sources of self-interstitial atoms, which may be a reason for the swelling of Pu after a period of self-radiation aging because of the higher concentration of vacancy in the bulk.

3.5 Release of He from surface

MD simulation are performed to investigate the release behavior of nanometer-size He bubble in nanometer-size δ Pu films which are often necessary to carry out microstructural characterization and surface analysis. Spherical voids with different size and depth d are created by removing Pu atoms and then He bubbles are formed with different He-vacancy atomic ratio η and diameter D by filling He atoms into the voids. D from about 1.25nm to 2.20nm, η from 1:1 to 4:1, d from 1.61nm to 5.56nm and temperatures T from 100K to 1200K (liquid Pu) are considered, respectively. In general, the similar trends of the simulation results with different model parameters (D , η , d and T) are observed, therefore only some representative results and the trends are discussed in the article.

3.5.1 He release process

All the simulation cases contain only one isolated He bubble and the bubble-bubble interactions are not fully taken into considerations. He bubble is initially placed in the center of the slab and thus its states and behaviors are similar to that in the bulk. The bubble with roughly spherical shape is clearly shown after initial MD relaxation and the shape can be kept during the complete process of MD simulation. The spherical shape can be interpreted by the isotropic crystal stresses bearing on He bubble, which was also found in other theoretical works. However, the diameter of the He bubble gradually increases before MD equilibrium and the distortion of the Pu atoms surrounding He bubble consequently occurs. The simulation results indicate that there is a critical model parameter for He release from the slab when other three parameters are fixed. Here, we put our efforts to the dependence of d on He release. The spherical shape of He bubble begins to distort with decreasing d as a result of anisotropic crystal stresses induced by surface stresses. When d reaches its critical value which is 1.85nm observed in this research, He atoms start releasing from the slab.

He release process is illustrated in Fig. 13 and can be briefly described as follows. Initial spherical shape of He bubble begins to elongate obviously towards the surface and push the surface Pu atoms away from the normal surface sites. The surface is gradually deformed and ruptured and a surface cavity connecting to the bulk is formed. As a result, the channel for He release is preliminary created, which induces the onset of He release. He atoms begin to release along the channel one by one at a relatively low rate. Simultaneously, the channel firstly expands with the evolution of MD simulation, which facilitates or accelerates He release. In other words, He release rate increases drastically

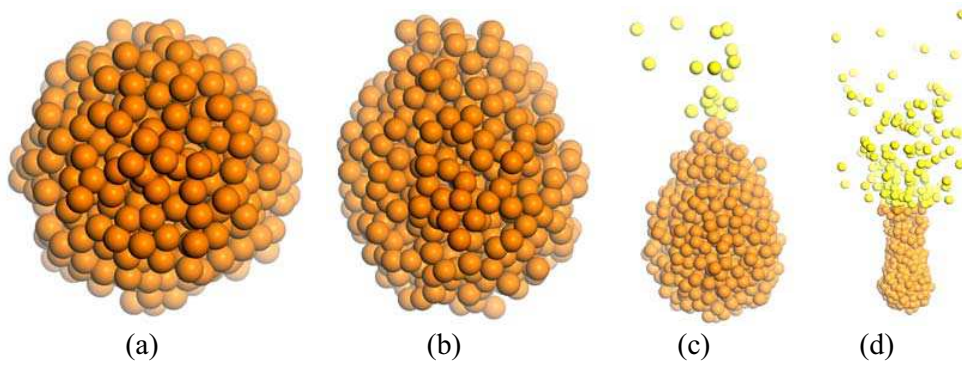


Figure 13: Side view of atomic configurations of He bubble during the process of He release ($d = 1.85\text{nm}$, $D = 2.20\text{nm}$, $\eta = 2.25$, $T = 310\text{K}$). The yellow balls denote the released He atoms and all the Pu atoms are not displayed in the configurations. (a) $t = 2\text{ps}$; (b) $t = 4\text{ps}$; (c) $t = 9\text{ps}$; (d) $t = 11\text{ps}$.

with the expansion of the channel and reaches the maximal release rate corresponding to the maximal expansion of the channel.

3.5.2 He release rate

In order to better understand the processes and the trends of He release, time-dependent relationships of He release fraction θ and release rate ν for some selected simulation cases are provided, as shown in Fig. 14. Three-stage characteristics of He release, i.e., accelerating, decelerating and terminable release are approximately exhibited. It is obvious that θ , ν and the interval time Δt from initial release to maximal ν of each stage are dependant on the model parameters. On the whole, the maximal θ and maximal ν increase with

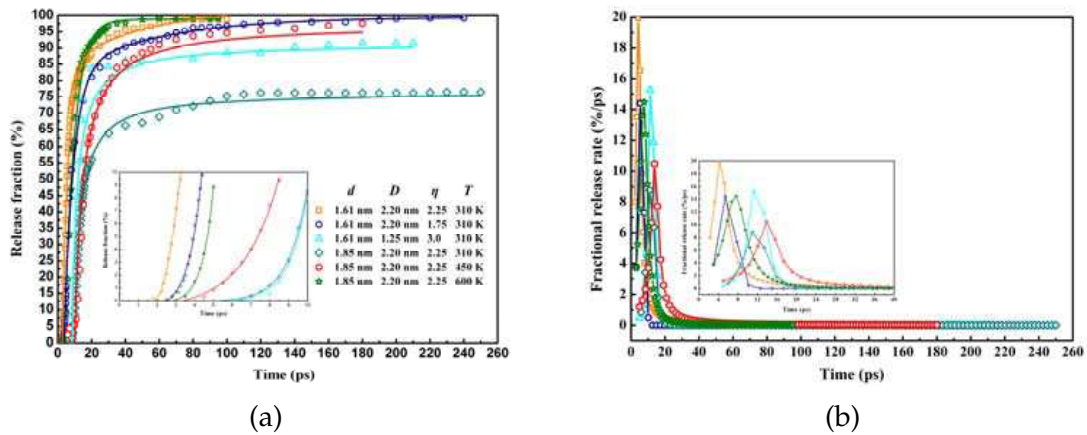


Figure 14: He release fraction and release rate from some selected computational models. (a) He release fraction as a function of simulation time. Inset is the initial release process with the release fraction limit to 10% and the time limit to 10ps. (b) He release rate differentiated from He release fraction as a function of simulation time. Inset is the initial release rate with the time limit to 20ps.

decreasing d and increasing D , η and T , but the trend of Δt is inverse. It is of interest to note that Δt of the simulation case ($D \approx 2.20\text{nm}$, $\eta = 2.25$, $d = 1.85\text{nm}$, $T = 310\text{K}$) is shorter than that of the simulation case with the same model parameters except for $T = 450\text{K}$. As is well known, He behaviors in materials are very sensitive to temperature [41]. According to our theoretical works, moderate temperature ($T < 0.5T_m$, where the melting point T_m equals to 913K for Pu) is favorable for the nucleation of He_nV_m cluster, which may partially account for the anomalous trend of Δt in the two cases discussed above.

Since there is almost no direct experimental and theoretical data on He release from Pu and radiation damages are not be considered in the present simulation, we turn to properly refer to the extensively-studied mechanisms of He release from metal tritides in which radiation damages can be also viewed as insignificant. Observations from metal tritides have indicated that He release process always consists of three stages and there is a critical He concentration for the onset of accelerating release [48,49]. The duration of each stage and the critical concentration are dependent on the inherent material properties, tritium content (approximately proportional to He content with age), temperature, sample shape and so on. The behaviors of He release generally have the same trends as observed in the present simulation with some exceptions mainly due to the differences in the states of He atoms or He bubbles. Unlike the metal tritides, in the simulation cases He bubbles are artificially created and fixed in the slab, so the influences of He bubble formation and additional He atoms are not considered for He release. As a result, He release from Pu reaches the accelerating stage relatively more rapidly than from metal tritides and He release can be viewed as terminable when the largest fractional He atoms release, as shown in Fig. 14 and the insets therein. Moreover, it is noticeable to point out that He release rates in metal films are much greater than that in bulk crystals, which means there exists a He bubble free region or denuded region corresponding to the critical d in the present simulations. Outside the denuded region, He bubble is retained in the host metal, whereas it expands rapidly and finally cracks, creating the channel for He atoms to propagate to the surface as long as they enter into the denuded region. However, due to the limits of model size and simulation time in the MD technique, the predicted d is much smaller than the measured thickness of denuded region which is approximately 15nm for erbium (Er) tritide films [50].

4 Conclusions

In this work, we present our recent theoretical findings on He effects in Pu during its self-radiation-damage process mainly by MD simulation technique. A modified EAM potential of Pu is developed by fitting its experimental lattice and solid parameters and proven to be effective to a certain extent to reproduce many solid properties of Pu. Some inherent mechanisms and macroscopical changes induced by He are discussed.

The processes of initial nucleation and growth of He bubble can be regarded as the continuous absorption of He atoms and vacancies by small He_nV_m clusters, which can be

deduced by the energetic calculation on the clusters formation energies and binding energies of point defects (He, vacancy and SIA). Progressive growth of He_nV_m clusters can eventually evolve as visible He bubbles. He bubble's growth can also be dominated by the mechanism of punching out of dislocation loop when the ratio of He-vacancy in the He_nV_m cluster is sufficiently high. In addition, grain boundaries give rise to an energetically favorable zone for the interstitial He atom accumulation and He bubble formation. As for the macroscopical aspects of He bubble, the swelling induced by He bubble is very small and less serious than other possible mechanism, such as void swelling. Moreover, the process of He release can be identified as the formation of release channel induced by the cracking of He bubble and surface structure.

Acknowledgments

This work was supported by the National Natural Science Foundation of China (Grant No. 20801007).

References

- [1] R. Jeanloz, Science-based stockpile stewardship, *Phys. Today*, 12 (2000), 44–49.
- [2] W. G. Wolfer, Radiation effects in plutonium, *Los Alamos Sci.*, 26 (2000), 274–285.
- [3] D. Dooley, B. Martinez, D. Olson, D. Olivas, R. Ronquillo and T. Rising, Diffusion of helium in plutonium alloys, in *Plutonium Future-The Science 2000* (K. K. S. Pillay and K. C. Kim, editors), pages 428–430, American Institute of Physics, 2000.
- [4] B. D. Wirth, A. J. Schwartz, M. J. Fluss, M. J. Caturla, M. A. Wall and W. G. Wolfer, Fundamental properties of Pu aging, *MRS Bull.*, 26 (2001), 679–683.
- [5] A. J. Schwartz, M. A. Wall, T. G. Zocco and W. G. Wolfer, Characterization and modelling of helium bubbles in self-irradiated plutonium alloys, *Philos. Mag.*, 85 (2005), 479–488.
- [6] P. Asoka-Kumar, S. Glade, P. A. Sterne and R. Howell, Evolution of defects in Pu during isochronal annealing and self-irradiation, in *Plutonium Futures-The Science 2003* (G. D. Jarvinen, editor), pages 121–122, American Institute of Physics, 2003.
- [7] C. Thiebaut, N. Baclet, B. Ravat, P. Giraud and P. Julia, Effect of radiation on bulk swelling of plutonium alloys, *J. Nucl. Mater.*, 361 (2007), 184–191.
- [8] S. M. Valone, M. I. Baskes, M. Stan, T. E. Mitchell, A. C. Lawson and K. E. Sickafus, Simulations of low energy cascades in fcc Pu metal at 300K and constant volume, *J. Nucl. Mater.*, 324 (2004), 41–51.
- [9] S. M. Valone and M. I. Baskes, Self-irradiation cascade simulations in plutonium metal: model behavior at high energy, *J. Computer-Aided Mater. Des.*, 14 (2007), 357–365.
- [10] S. M. Valone, M. I. Baskes and R. L. Martin, Atomistic model of helium bubbles in gallium-stabilized plutonium alloys, *Phys. Rev. B*, 73 (2006), 214209.
- [11] V. Dremov, P. Sapozhnikov, A. Kutepov, V. Anisimov, M. Korotin, A. Shorikov, D. L. Preston and M. A. Zocher, Atomistic simulations of helium dynamics in a plutonium lattice, *Phys. Rev. B*, 77 (2008), 224306.
- [12] B. Y. Ao, J. Y. Yang, X. L. Wang and W. Y. Hu, Atomistic behavior of helium-vacancy clusters in aluminum, *J. Nucl. Mater.*, 350 (2006), 83–88.

- [13] B. Y. Ao, X. L. Wang, W. Y. Hu, J. Y. Yang and J. X. Xia, Atomistic study of small helium bubbles in plutonium, *J. Alloys Comp.*, 444-445 (2007), 300-304.
- [14] B. Y. Ao, X. L. Wang, W. Y. Hu and J. Y. Yang, Molecular dynamics simulation of helium-vacancy interaction in plutonium, *J. Nucl. Mater.*, 385 (2009), 75-78.
- [15] M. S. Daw and M. I. Baskes, Embedded-atom method: derivation and application to impurities, surfaces and other defects in metals, *Phys. Rev. B*, 29 (1984), 6443-6453.
- [16] M. I. Baskes, Modified embedded-atom potentials for cubic materials and impurities, *Phys. Rev. B*, 46 (1992), 2727-2742.
- [17] Y. Ouyang, B. Zhang, S. Liao and Z. Jin, A simple analytical EAM model for bcc metals including Cr and its application, *Z. Phys. B*, 101 (1996), 161-168.
- [18] H. Deng, W. Hu, X. Shu and B. Zhang, Atomistic simulation of the segregation profiles in Mo-Re random alloys, *Surf. Sci.*, 543 (2003), 95-102.
- [19] J. Yang, W. Hu, H. Deng and D. Zhao, Temperature dependence of atomic relaxation and vibrations for the vicinal Ni(9 7 7) surface: a molecular dynamics study, *Surf. Sci.*, 572 (2004), 439-448.
- [20] W. Hu, B. Zhang, B. Huang, F. Gao and D. J. Bacon, Analytic modified embedded atom potentials for HCP metals, *J. Phys. Condens. Matter*, 13 (2001), 1193.
- [21] W. Hu, H. Deng and M. Fukumoto, Point-defect properties in HCP rare earth metals with analytic modified embedded atom potentials, *Euro. Phys. J. B*, 34 (2003), 429-440.
- [22] W. Hu, X. Shu and B. Zhang, Point-defect properties in body-centered cubic transition metals with analytic EAM interatomic potentials, *Comput. Mater. Sci.*, 23 (2002), 175-189.
- [23] W. Hu and M. Fukumoto, The application of the analytic embedded atom potential to alkali metal, *Modell. Simula. Mater. Sci.*, 10 (2002), 707-726.
- [24] R. A. Johnson, Phase stability of fcc alloys with the embedded-atom method, *Phys. Rev. B*, 41 (1990), 9717-9720.
- [25] P. Pochet, Modeling of aging in plutonium by molecular dynamics, *Nucl. Instr. Meth. Phys. Res. B*, 202 (2003), 82-87.
- [26] M. I. Baskes, Atomistic model of plutonium, *Phys. Rev. B*, 62 (2000), 15532-15537.
- [27] X. Dai, S. Y. Savrasov, G. Kotliar, A. Migliori, H. Ledbetter and E. Abrahams, Calculated phonon spectra of plutonium at high temperatures, *Science*, 300 (2003), 953-955.
- [28] F. J. Cherne, M. I. Baskes and B. L. Holian, Predicted transport properties of liquid plutonium, *Phys. Rev. B*, 67 (2003), 092104.
- [29] M. J. Fluss, B. D. Wirth, M. Wall, T. E. Felter, M. J. Caturla, A. Kubota and T. Diaz de la Rubia, Temperature-dependent defect properties from ion-irradiation in Pu (Ga), *J. Alloys Comp.*, 368 (2004), 62-74.
- [30] M. I. Baskes, K. Muralidharan, M. Stan, S. M. Valone and F. J. Cherne, Using the modified embedded-atom method to calculate the properties of Pu-Ga alloys, *JOM*, 9 (2003), 41-50.
- [31] J. Wong, M. Krisch, D. L. Farber, F. Ocelli, A. J. Schwartz, T. C. Chiang, M. Wall, C. Boro and R. Xu, Phonon dispersions of fcc δ -Plutonium-Gallium by inelastic X-ray scattering, *Science*, 301 (2003), 1078-1080.
- [32] R. A. Johnson, Empirical potentials and their use in the calculation of energies of point defects in metals, *J. Phys. F: Metal Phys.*, 3 (1973), 295.
- [33] M. I. Baskes and C. F. Melius, Pair potentials for fcc metals, *Phys. Rev. B*, 20 (1979), 3197-3204.
- [34] S. M. Valone, M. I. Baskes and R. L. Martin, LA-UR-02-1958, Los Alamos National Laboratory, 2002.
- [35] P. H. Chen, X. L. Wang, X. C. Lai, G. Li, B. Y. Ao and Y. Long, *Ab initio* interionic potentials

- for UN by multiple lattice inversion, *J. Nucl. Mater.*, 404 (2010), 6–8.
- [36] P. H. Chen, X. C. Lai, K. Z. Liu, X. L. Wang, B. Bai, B. Y. Ao and Y. Long, Development of a pair potential for Fe-He by lattice inversion, *J. Nucl. Mater.*, 405 (2010), 156–159.
- [37] H. Trinkaus, Radiation effects and defects in solids, *Radiat. Eff.*, 78 (1983), 189–211.
- [38] K. Morishita, R. Sugano and B. D. Wirth, MD and KMC modeling of the growth and shrinkage mechanisms of helium-vacancy clusters in Fe, *J. Nucl. Mater.*, 323 (2003), 243–250.
- [39] J. B. Adams and W. G. Wolfer, Formation energies of helium-void complexes in nickel, *J. Nucl. Mater.*, 166 (1989), 235–242.
- [40] M. Parrinello and A. Rahman, Crystal structure and pair potentials: a molecular-dynamics study, *Phys. Rev. Lett.*, 45 (1980), 1196–1199.
- [41] H. Trinkaus and B. N. Singh, Helium accumulation in metals during irradiation—where do we stand?, *J. Nucl. Mater.*, 323 (2003), 229–242.
- [42] J. Xia, W. Hu, J. Yang, B. Ao and X. Wang, A comparative study of helium atom diffusion via an interstitial mechanism in nickel and palladium, *Phys. Stat. Sol.*, 243 (2006), 579–583.
- [43] A. B. Adams and W.G. Wolfer, On the diffusion mechanisms of helium in nickel, *J. Nucl. Mater.*, 158 (1988), 25–29.
- [44] T. G. Zocco, Transmission electron microscopy of plutonium alloys, *Los Almos Sci.*, 26 (2000), 286–289.
- [45] M. I. Baskes and V. Vitek, Trapping of hydrogen and helium at grain boundaries in nickel: an atomistic study, *Met. Trans. A*, 16 (1985), 1625–1631.
- [46] R. J. Kurtz and H. L. Heinisch, The effects of grain boundary structure on binding of He in Fe, *J. Nucl. Mater.*, 329-333 (2004), 1199–1203.
- [47] W. G. Wolfer, The pressure for dislocation loop punching by a single bubble, *Phil. Mag. A*, 58 (1988), 285–297.
- [48] R. G. Spulak, On helium release from metal tritides, *J. Less-Common. Metals*, 132 (1987), L17–L20.
- [49] W. J. Camp, Helium detrapping and release from metal tritides, *J. Vac. Sci. Tech.*, 14 (1977), 514–517.
- [50] C. S. Snow and L. N. Brewer, Helium release and microstructural changes in $\text{Er(D,T)}_{2-x}^3\text{He}_x$ films, *J. Nucl. Mater.*, 374 (2008), 147–157.